RSC Advances

PAPER

View Article Online
View Journal | View Issue

Cite this: *RSC Adv.*, 2021, **11**, 19797

Two-dimension on two-dimension growth: hierarchical $Ni_{0.2}Mo_{0.8}N$/Fe-doped Ni_3N nanosheet array for overall water splitting†

Chen Liu, Han Zhu, * Shuanglong Lu, Fangping Xu, Fang Duan and Mingliang Du *

Received 17th February 2021
Accepted 24th May 2021

DOI: 10.1039/d1ra01299a

rsc.li/rsc-advances

Developing advanced electrocatalysts with low cost for electrocatalytic water splitting are highly desirable. Herein, we report the design of two-dimension on two-dimension growth of hierarchical $Ni_{0.2}Mo_{0.8}N$ nanosheets on Fe-doped Ni_3N nanosheets supported on Ni foam ($Ni_{0.2}Mo_{0.8}N$/Fe–Ni_3N/NF) *via* hydrothermal reaction and nitridation treatment. In the hierarchical structures, small $Ni_{0.2}Mo_{0.8}N$ nanosheets were uniformly anchored on Fe–Ni_3N nanosheets. Due to enhanced electron transfer between $Ni_{0.2}Mo_{0.8}N$ and Fe–Ni_3N, $Ni_{0.2}Mo_{0.8}N$/Fe–Ni_3N/NF exhibits superior electrocatalytic activity for the oxygen evolution reaction (OER) and the hydrogen evolution reaction (HER). After stability tests for 50 h, $Ni_{0.2}Mo_{0.8}N$/Fe–Ni_3N/NF exhibits negligible degradation of the current density for the OER (91% remain) and HER (95% remain), suggesting excellent stability. Owing to the outstanding performance, $Ni_{0.2}Mo_{0.8}N$/Fe–Ni_3N/NF display a cell voltage of 1.54 V (10 mA cm^{-2}) for electrocatalytic overall water splitting.

Introduction

Hydrogen (H_2) is a promising and attractive energy source owing to its high combustion efficiency, non-polluting production and sustainability.[1–3] Currently, the industrial methods to produce H_2 usually consume a lot of fossil energy, and are unfavorable for solving the problems of energy and the environment.[4–6] Thus, production of H_2 through efficient and facile methods are highly desirable. Electrocatalytic water splitting is an exciting strategy to sustainably produce hydrogen energy.[7–10] Electrochemical water splitting consists of two half-reaction steps, the oxygen evolution reaction (OER) and the hydrogen evolution reaction (HER), requiring higher overpotentials to obtain significant catalytic efficiency due to the existence of inherent energy barriers.[11–14] Therefore, electrocatalysts are crucial to reduce the energy barrier of rate-determining steps. Pt-based noble metals are the best catalysts towards the OER and HER.[15–18] However, their lower abundance and higher cost greatly suppress their wide commercial development. Therefore, exploring highly efficient and earth-abundant electrocatalysts toward water splitting are vital for large-scale practical application.

Nowadays, transition metal-based materials[19–21] including the chalcogenides,[22–24] phosphides,[25–27] nitrides,[28–30] carbides[31–33] and selenides[34–36] have been extensively applied for electrocatalysis. Among of these electrocatalysts, transition metal nitrides (TMNs) are the new emerging alternative electrocatalyst for water splitting due to the high electrical conductivity and corrosion-resistance.[37–39] However, amounts of electrocatalysts with highly performance are only suitable for OER or HER. Therefore, developing outstanding bifunctional electrocatalysts with excellent activity for OER and HER is crucial. Integrating multiple metal into one integrated material provide a powerful way to turn the electronic structure, further improving the OER and HER activity.[40–43]

Herein, we reported the design of two-dimension on two-dimension growth of hierarchical $Ni_{0.2}Mo_{0.8}N$ nanosheets on Fe-doped Ni_3N nanosheets supported on Ni foam ($Ni_{0.2}Mo_{0.8}N$/Fe–Ni_3N/NF). In the hierarchical structures, small $Ni_{0.2}Mo_{0.8}N$ nanosheets were homogenously distributed on Fe–Ni_3N nanosheets. The $Ni_{0.2}Mo_{0.8}N$/Fe–Ni_3N/NF exhibits lowest OER overpotential of 266 mV (20 mA cm^{-2}), compared with the Fe–Ni_3N/NF (292 mV), $Ni_{0.2}Mo_{0.8}N$/NF (320 mV) and commercial RuO_2 (328 mV). The $Ni_{0.2}Mo_{0.8}N$/Fe–Ni_3N/NF shows negligible degradation of the current density (91%) after OER stability test for 50 h. In addition, the $Ni_{0.2}Mo_{0.8}N$/Fe–Ni_3N/NF also displays the lower overpotential (40 mV, 20 mA cm^{-2}) and excellent durability (50 h, 95% current density remain). The $Ni_{0.2}Mo_{0.8}N$/Fe–Ni_3N/NF shows a quite low cell voltage of 1.54 V (10 mA cm^{-2}) for overall water splitting.

Experimental

Chemicals

Iron nitrate nonahydrate ($Fe(NO_3)_3 \cdot 9H_2O$), sodium molybdate ($Na_2(MoO_4)_2 \cdot H_2O$), urea, ammonium fluoride (NH_4F), nickel

Key Laboratory of Synthetic and Biological Colloids, Ministry of Education, School of Chemical and Material Engineering, Jiangnan University, Wuxi 214122, P. R. China. E-mail: zhysw@jiangnan.edu.cn; du@jiangnan.edu.cn

† Electronic supplementary information (ESI) available. See DOI: 10.1039/d1ra01299a

nitrate hexahydrate ($Ni(NO_3)_2 \cdot 6H_2O$), ethanol, and ruthenium dioxide (RuO_2) were obtained from Sinopharm Chemical Reagent Co. Ltd. Potassium hydroxide (KOH) and Commercial 20% Pt/C were purchased from Shanghai Macklin Biochemical Co. Ltd. The 5 wt% Nafion solution was obtained from Sigma Aldrich. Ni foam (NF) was brought from Kunshan Rongsheng company, China. Unless otherwise stated, all reagents were used without purification.

Synthesis of $NiMoO_4$ and $Ni_{0.2}Mo_{0.8}N$ grown on NF ($NiMoO_4$/NF and $Ni_{0.2}Mo_{0.8}N$/NF)

The $NiMoO_4$ supported on NF were synthesized by the hydrothermal reaction. 2 mmol $Ni(NO_3)_2 \cdot 6H_2O$ and 2 mmol $Na_2(MoO_4)_2 \cdot H_2O$ were dissolved in 17.5 mL distilled water, respectively. Then, the mixed solution were transfer to the Teflon-lined stainless steel autoclave and heated at 150 °C for 6 h. Then, after cooling down to 25 °C, the as-prepared $NiMoO_4$/NF materials were cleaned by the distilled water and keep ultrasonicate for 30 min. Furthermore, the $Ni_{0.2}Mo_{0.8}N$/NF were prepared by the following nitridation treatment.

The dry $NiMoO_4$/NF was placed at furnace and treated in a flow of 20 standard cubic centimeters (sccm) NH_3 and 130 sccm Ar. The $NiMoO_4$/NF kept at 500 °C for 1 h (5 °C min^{-1}). $Ni_{0.2}Mo_{0.8}N$/NF was obtained after the treatment.

Synthesis of Fe-doped $Ni(OH)_2$ precursor grown on NF and Fe-doped Ni_3N grown on NF

Fe-doped $Ni(OH)_2$ precursor grown on Ni foam (Fe–$Ni(OH)_2$/NF) was obtained to prepare the $Ni_{0.2}Mo_{0.8}N$/Fe–Ni_3N/NF. Before starting the reaction, the NF (2 × 3 cm^2) was pre-treated with HCl solution (1 M) to get rid of the oxidation layer on the NF. After 20 min, the NF was washed by distilled water. 0.2 mmol $Fe(NO_3)_3 \cdot 9H_2O$, 3.8 mmol $Ni(NO_3)_2 \cdot 6H_2O$, 10 mmol urea and 20 mL distilled water were mixed to form the homogeneous solution by a magnetic stirrer. The 4 mmol NH_4F and as-treated NF was immersed in the precursor solution and keep stirring for 30 min. Then the Teflon-lined stainless steel autoclave was used as the container of preparing the Fe–$Ni(OH)_2$/NF and heated at 120 °C for 14 h. After cooling down to 25 °C, the Fe–$Ni(OH)_2$/NF was cleaned by ultrasonicating with distilled water for 30 min and dried at 60 °C. Then the dry Fe–$Ni(OH)_2$/NF was placed at furnace and treated in a flow of 20 standard cubic centimeters (sccm) NH_3 and 130 sccm Ar. The Fe–$Ni(OH)_2$/NF kept at 500 °C for 1 h (5 °C min^{-1}). Fe–Ni_3N/NF was obtained after the treatment.

Fabrication of $Ni_{0.2}Mo_{0.8}N$/Fe-doped Ni_3N nanosheets arrays supported on NF and $Ni_{0.2}Mo_{0.8}N$ nanosheets arrays supported on NF

The $Ni_{0.2}Mo_{0.8}N$/Fe-doped Ni_3N arrays supported on NF ($Ni_{0.2}Mo_{0.8}N$/Fe–Ni_3N/NF) were synthesized through the combination of hydrothermal reaction and nitridation treatment. 2 mmol $Ni(NO_3)_2 \cdot 6H_2O$ and 2 mmol $Na_2(MoO_4)_2 \cdot H_2O$ were dissolved in 17.5 mL distilled water, respectively. The Fe–$Ni(OH)_2$/NF were immersed in mixed solution containing $Na_2(MoO_4)_2 \cdot H_2O$ and $Ni(NO_3)_2 \cdot 6H_2O$. After 30 min, the Fe–$Ni(OH)_2$/NF and mixed solution were transfer to the Teflon-lined stainless steel autoclave and heated at 150 °C for 6 h. Then, after cooling down to 25 °C, the as-prepared Fe–$Ni(OH)_2$/$NiMoO_4$/NF materials were cleaned by the distilled water and keep ultrasonicate for 30 min. The $Ni_{0.2}Mo_{0.8}N$/Fe–Ni_3N/NF was obtained through the NH_3 treatment of Fe–$Ni(OH)_2$/$NiMoO_4$/NF.

Characterization methods

The morphologies of the as-synthesized materials were examined by field emission scanning electron microscope (FE-SEM, S-4800, Hitachi, Japan) and transmission electron microscope (TEM, JEM-2010plus, JEOL, Japan). The phase structures were recorded by X-ray diffractometer (D8 Discover, Bruker AXS, Germany) with a Cu K_α radiation ($\lambda = 1.5406$ Å). Chemical states and composition of the as-synthesized materials were investigated by X-ray photoelectron spectroscopy (XPS, Axis supra, Kratos Analytical Ltd, UK). The results were obtained at 15 kV and 10 mA with monochromatic Al K_α radiation. All the XPS spectra of materials were corrected through C 1s spectrum at 284.8 eV.

Electrochemical measurement

The electrocatalytic performances of as-synthesized materials were performed by a CHI660E electrochemical workstation (Chen Hua, Shanghai, China). All the electrochemical tests were operated in 1 M KOH solution. The three-electrode system was used to perform the OER and HER tests. The as-prepared materials (geometric area: 0.5 cm^2) and a carbon rod were used as working electrode and counter electrode, respectively. Furthermore, the reference electrode was a saturated calomel electrode (SCE). The potential was corrected by the following equation: $E(\text{RHE}) = E(\text{SCE}) + 0.059\ \text{pH} + 0.244$.

The linear sweep voltammogram (LSV) for OER was measured in a potential range of 1.0 to 1.6 V *versus* RHE (*vs.* RHE). For HER measurements, the LSV was measured in a potential range of and 0 to −0.5 V *vs.* RHE. The scan rate is 1 mV s^{-1}. OER and HER curves of were treated by iR correction. According to the equation: $E_{\text{corrected}} = E_{\text{uncorrected}} - iR_s$, the curve of *iR* correction would be finished. R_s (solution resistance) was able to observed by the electrochemical impedance spectroscopy (EIS) tests. The EIS for OER and HER was tested at 1.47 V and −0.03 V *vs.* RHE from 10 kHz to 0.01 Hz with a 10 mV AC amplitude. The stability test for OER was operated at 1.515 V *vs.* RHE for 50 h. The stability test for HER was finished at −74 mV *vs.* RHE for 50 h. The double-layer capacitance (C_{dl}) was obtained by the CVs cycling tests from 0.1 to 0.2 V *vs.* RHE with scan rates ranged from 10–60 mV s^{-1}. C_{dl} can be used to calculate the electrochemically active surface area (ECSA). Overall water splitting was measured in a two-electrode electrolyzer. The LSV was measured in a potential range of 1.0 to 1.9 V voltage. The stability test of overall water-splitting was operated at 1.59 V voltage for 20 h.

Results and discussion

As shown in Fig. 1a–c, after the hydrothermal reaction, the Fe–$Ni(OH)_2$ nanosheets were densely and vertically grown on substrate Ni foam (NF), forming a unique three-dimensional

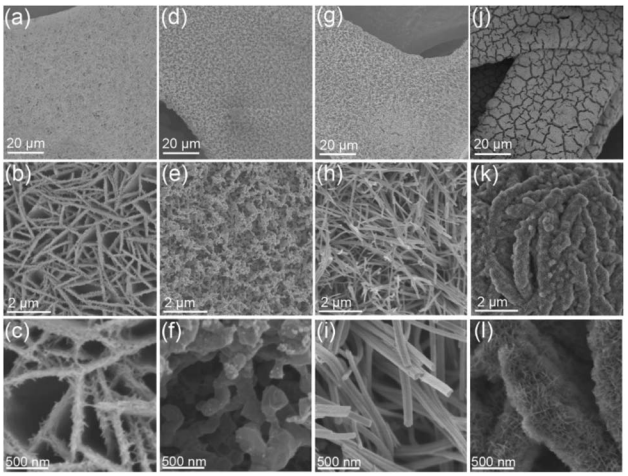

Fig. 1 FE-SEM images of (a–c) Fe–Ni(OH)$_2$/NF, (d–f) Fe–Ni$_3$N/NF, (g–i) Ni$_{0.2}$Mo$_{0.8}$N/NF and (j–l) Ni$_{0.2}$Mo$_{0.8}$N/Fe–Ni$_3$N/NF at different magnifications.

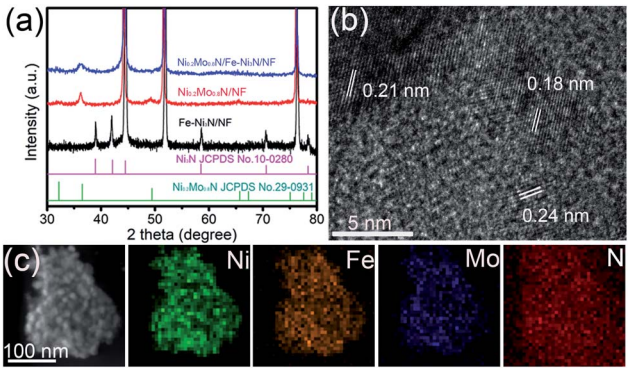

Fig. 2 (a) XRD patterns of Ni$_{0.2}$Mo$_{0.8}$N/Fe–Ni$_3$N/NF, Ni$_{0.2}$Mo$_{0.8}$N/NF and Fe–Ni$_3$N/NF. (b) HRTEM image of Ni$_{0.2}$Mo$_{0.8}$N/Fe–Ni$_3$N/NF. (c) STEM-EDS mapping images of Ni$_{0.2}$Mo$_{0.8}$N/Fe–Ni$_3$N/NF.

(3D) architectures. The thickness of the Fe–Ni(OH)$_2$ nanosheets ranged from 80–200 nm (Fig. S1†). After the NH_3 treatment at 500 °C, the Fe–Ni(OH)$_2$ were converted into Fe-doped Ni$_3$N (Fe–Ni$_3$N). The Fe–Ni(OH)$_2$ nanosheets were transformed into three-dimensional porous network structures consist of interconnected nanospheres (Fig. 1d–f). The average diameters of Fe–Ni$_3$N grains ranged from 160–320 nm (Fig. S1†). As shown in Fig. S2a–c,† the $NiMoO_4$ precursor nanowires were synthesized on NF through the same hydrothermal reaction. After the NH_3 treatment, the as-prepared Ni$_{0.2}$Mo$_{0.8}$N/NF also indicates the nanowire morphologies and structures (Fig. 1i).

The diameters of the Ni$_{0.2}$Mo$_{0.8}$N nanowires ranged from 80 to 200 nm (Fig. S1†). When $NiMoO_4$ meets Fe–Ni(OH)$_2$ (Fig. S2d–f†), the as-synthesized $NiMoO_4$/Fe–Ni(OH)$_2$/NF exhibited a hierarchical structure consist of Fe–Ni(OH)$_2$ as substrates and $NiMoO_4$ vertically grown on Fe–Ni(OH)$_2$ nanosheets. Through the NH_3 treatment at 500 °C, the $NiMoO_4$/Fe–Ni(OH)$_2$/NF were converted into Ni$_{0.2}$Mo$_{0.8}$N/Fe–Ni$_3$N/NF (Fig. 1j–l) with two unique phases. The Fe–Ni$_3$N nanosheets were coated by small Ni$_{0.2}$Mo$_{0.8}$N nanosheets. It is interesting that with the Ni$_{0.2}$Mo$_{0.8}$N, the Fe–Ni$_3$N substrates still remain the morphology of $NiMoO_4$/Fe–Ni(OH)$_2$. The thickness of Ni$_{0.2}$Mo$_{0.8}$N/Fe–Ni$_3$N/NF ranged from 210–350 nm (Fig. S3a and b†), while the thickness range of small nanosheet is 7–15 nm (Fig. S3c and d†). Different from the individual Fe–Ni$_3$N (Fig. 1d–f), Fe–Ni$_3$N substrates were not also transformed into the similar structure. The small Ni$_{0.2}$Mo$_{0.8}$N nanosheets could hinder the collapse of Fe–Ni$_3$N from nanosheets to interconnected nanospheres. The unique structure of Ni$_{0.2}$Mo$_{0.8}$N/Fe–Ni$_3$N/NF may be provide more active sites for electrocatalysis.

The crystal structures of materials were investigated by the XRD characterization. Fig. 2a and S4† show the sharp peaks near the 44.5°, 51.8° and 76.4°, corresponding to the metal Ni in the NF. The peaks of Fe–Ni(OH)$_2$/NF were observed at 33.5°, 34.4° and 38.8° (Fig. S4†), indicating the formation of Ni(OH)$_2$ phase (JCPDS 38-0715). The peaks at 38.9°, 42.1°, 58.5°, 70.6° and 78.4° of Fe–Ni$_3$N/NF (Fig. 2a) were assigned to Ni$_3$N phases (JCPDS 10-0280), indicating that the Ni(OH)$_2$/NF were transformed to Fe–Ni$_3$N phases after NH_3 treatment. The visible diffraction peaks of Ni$_{0.2}$Mo$_{0.8}$N/NF at 32.2°, 36.5° and 49.4° belong to the crystal planes of Ni$_{0.2}$Mo$_{0.8}$N (JCPDS 29-0931). For the Ni$_{0.2}$Mo$_{0.8}$N/Fe–Ni$_3$N/NF, the peaks for Ni$_3$N phases were very weak due to the low crystallinity, while the peaks for Ni$_{0.2}$Mo$_{0.8}$N phases are strong. The HRTEM image of Fe–Ni$_3$N/NF reveals a lattice fringe (0.20 nm) (Fig. S5a and b†), corresponding to the (100) plane of Ni$_3$N. The TEM image of Ni$_{0.2}$Mo$_{0.8}$N/Fe–Ni$_3$N/NF (Fig. S5c†) indicates that small Ni$_{0.2}$Mo$_{0.8}$N nanosheets were uniformly dispersed on Fe–Ni$_3$N/NF nanosheets. Fig. 2b shows the HRTEM image of Ni$_{0.2}$Mo$_{0.8}$N/Fe–Ni$_3$N/NF. The (100) and (101) planes of Ni$_{0.2}$Mo$_{0.8}$N was observed. Furthermore, the (002) plane (the interplanar distance of 0.21 nm) of Ni$_3$N was observed in Fig. 2b. There were no peaks of metal Fe or Fe oxides and nitrides in the measured XRD patterns and HRTEM images, indicating that the Fe elements were doped into the Ni(OH)$_2$ and the Ni$_3$N crystal matrix.[44–46] The STEM-EDS mapping images of Ni$_{0.2}$Mo$_{0.8}$N/Fe–Ni$_3$N/NF were represented in Fig. 2c. As shown in new Fig. 2c, the Ni, Mo, Fe and N were uniformly distributed throughout the randomly examined Ni$_{0.2}$Mo$_{0.8}$N/Fe–Ni$_3$N nanosheets. The Fe, Ni and N elements can be visible observed as substrates while the Ni, Mo and N elements also distributed as spots. The results confirmed the formation of hierarchical structures of Ni$_{0.2}$Mo$_{0.8}$N/Fe–Ni$_3$N/NF using Fe–Ni$_3$N as support.

XPS spectra were shown in Fig. S6† and 3 to research the chemical compositions and surface chemical states of materials. Fig. S6† is the XPS survey of Ni$_{0.2}$Mo$_{0.8}$N/Fe–Ni$_3$N/NF, indicating that the Ni, Fe, Mo and N were observed. In Fig. 3a, the two peaks of the Ni$_{0.2}$Mo$_{0.8}$N/Fe–Ni$_3$N/NF at 852.6 and 870.2 eV belong to the Ni species in Ni–N bonds.[47–49] Furthermore, the peaks located at 855.6, 873.5 eV and 857.1, 876.3 eV correspond to the oxidized Ni^{2+} and Ni^{3+} species, while the remaining two peaks (880.1 and 861.8 eV) belong to satellite peaks.[50,51] Compared with the BE of Ni$_{0.2}$Mo$_{0.8}$N/NF, the binding energy (BE) values of Ni–N bond of Ni$_{0.2}$Mo$_{0.8}$N/Fe–Ni$_3$N/NF shifts negatively by about 0.2 eV (Fig. 3a). The difference in

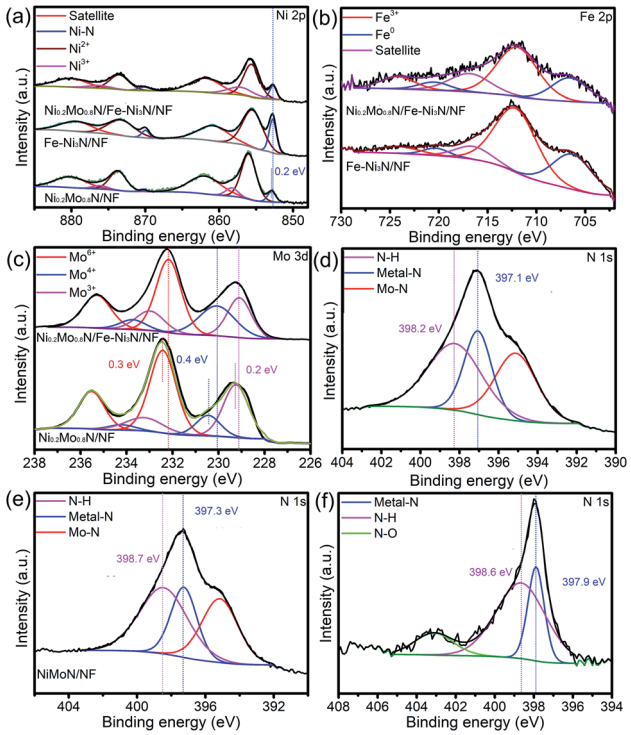

Fig. 3 (a) Ni 2p XPS spectra of $Ni_{0.2}Mo_{0.8}N$/Fe–Ni_3N/NF, Fe–Ni_3N/NF and $Ni_{0.2}Mo_{0.8}N$/NF. (b) Fe 2p XPS spectra of $Ni_{0.2}Mo_{0.8}N$/Fe–Ni_3N/NF and Fe–Ni_3N/NF. (c) Mo 3d XPS spectra $Ni_{0.2}Mo_{0.8}N$/Fe–Ni_3N/NF and $Ni_{0.2}Mo_{0.8}N$/NF. (d–f) N 1s XPS spectra of $Ni_{0.2}Mo_{0.8}N$/Fe–Ni_3N/NF, $Ni_{0.2}Mo_{0.8}N$/NF and Fe–Ni_3N/NF.

BEs of the Ni–N bond between the $Ni_{0.2}Mo_{0.8}N$/Fe–Ni_3N/NF and Fe–Ni_3N/NF might be attributed to the electron interaction between the Fe–Ni_3N nanosheets and $Ni_{0.2}Mo_{0.8}N$ nanosheets or the interaction with underlying NF substrates.

The BEs shift in Mo 3d suggests the strong electron transfer from the $Ni_{0.2}Mo_{0.8}N$ to Fe–N_3N, leading to the strong interaction between the two phases. Fig. 3d shows the N 1s XPS spectra $Ni_{0.2}Mo_{0.8}N$/Fe–Ni_3N/NF, the peak at about 397.1 eV corresponds to the N species of transition metal–N bonds, while the peak at about 395.2 eV was attributed to Mo–N bonds.[53] The peak at 398.2 eV belongs to the N–H species on the surface of materials.[54] Fig. 3e and f represented the N 1s XPS spectra of $Ni_{0.2}Mo_{0.8}N$/NF and Fe–Ni_3N/NF. By analyzing the peak in Fig. 3d and f, the negative shift in BEs of the $Ni_{0.2}Mo_{0.8}N$/Fe–Ni_3N/NF was observed. The changes in BEs of N 1s of $Ni_{0.2}Mo_{0.8}N$/Fe–Ni_3N/NF suggests that the Fe–Ni_3N integrated with $Ni_{0.2}Mo_{0.8}N$ can lead to the enhanced charge transfers and electron interactions.

The OER performance of samples was examined. As shown in Fig. 4a and b, the $Ni_{0.2}Mo_{0.8}N$/Fe–Ni_3N/NF displays the overpotential of 266 mV to acquire 20 mA cm^{-2}. The overpotentials of $Ni_{0.2}Mo_{0.8}N$/NF (320 mV), Fe–Ni_3N/NF (292 mV) and commercial RuO_2 (328 mV) are higher than those of the $Ni_{0.2}Mo_{0.8}N$/Fe–Ni_3N/NF. Fig. 4c shows the Tafel slopes of electrocatalysts. The $Ni_{0.2}Mo_{0.8}N$/Fe–Ni_3N/NF had the lowest Tafel slopes (54 mV dec^{-1}), indicating the best OER performance than those of the Fe–Ni_3N/NF, $Ni_{0.2}Mo_{0.8}N$/NF and commercial RuO_2, respectively. In addition, the performances of $Ni_{0.2}Mo_{0.8}N$/Fe–Ni_3N/NF was superior to those of recently reported OER catalysts (Table S1†).

EIS measurements were performed to analyze the OER electrode kinetics. In the Nyquist plots (Fig. 4d), the $Ni_{0.2}Mo_{0.8}N$/Fe–Ni_3N/NF reveals a small charge transfer resistance (R_{ct}) of 4.4 Ω. The R_{ct} of Fe–Ni_3N/NF and $Ni_{0.2}Mo_{0.8}N$/NF is 10.6 Ω and 26.9 Ω, respectively. The relatively lower Tafel slope and R_{ct} suggests the fast kinetics process of $Ni_{0.2}Mo_{0.8}N$/Fe–Ni_3N/NF. The combination of Fe–Ni_3N and $Ni_{0.2}Mo_{0.8}N$ nanosheets lead to the superior OER activity.

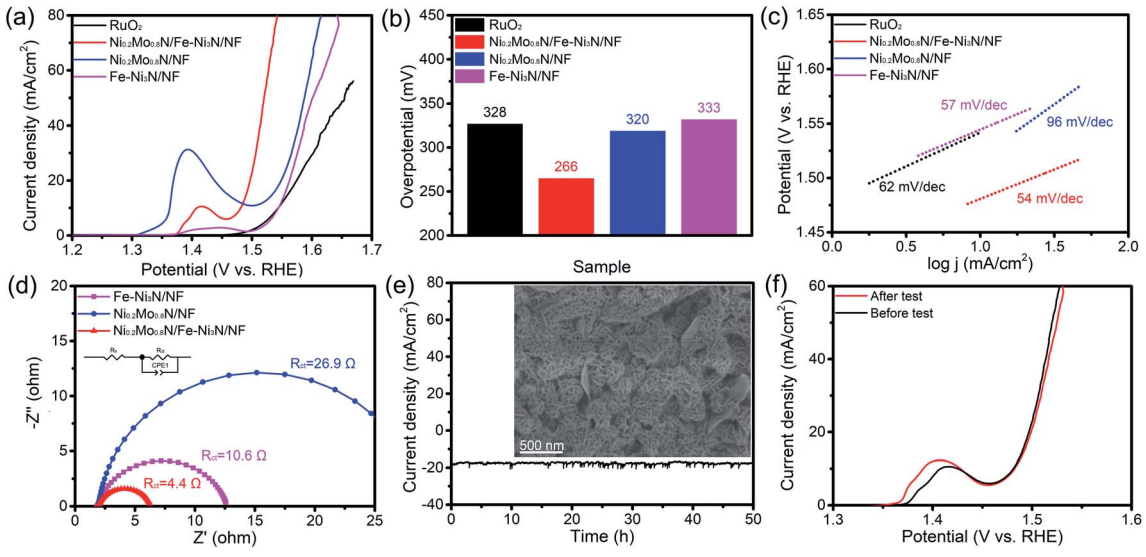

Fig. 4 (a) OER polarization curves of various catalysts. (b) The overpotential of the catalysts obtained at current density of 20 mA cm^{-2}. (c) Tafel slopes of catalysts. (d) EIS spectra of various catalysts recorded at potential of 1.47 V *vs.* RHE. (e) The current–time curves of $Ni_{0.2}Mo_{0.8}N$/Fe–Ni_3N/NF for OER. Inset is the FE-SEM image of $Ni_{0.2}Mo_{0.8}N$/Fe–Ni_3N/NF after OER stability test. (f) The polarization curves of $Ni_{0.2}Mo_{0.8}N$/Fe–Ni_3N/NF before and after stability test for 50 h.

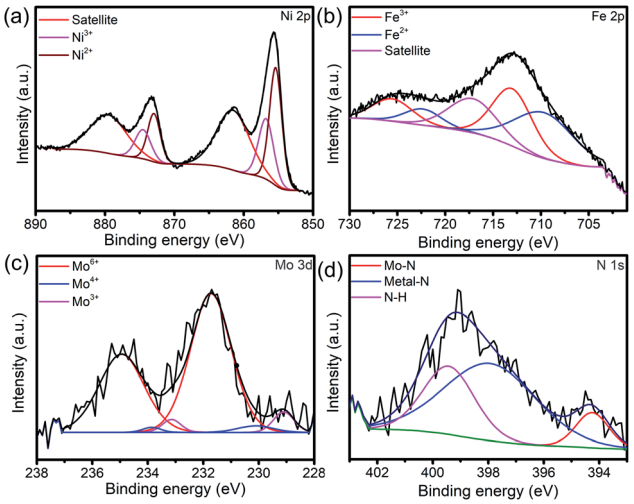

Fig. 5 (a) Ni 2p, (b) Fe 2p, (c) Mo 3d and (d) N 1s XPS spectra of $Ni_{0.2}Mo_{0.8}N$/Fe–Ni_3N/NF after OER stability test for 50 h.

The stability test was carried out by chronopotentiometry measurement to investigate the changes of the $Ni_{0.2}Mo_{0.8}N$/Fe–Ni_3N/NF catalyst after prolonged water electrolysis. Fig. 4e shows the current–time curves of OER chronopotentiometry test. The current density of $Ni_{0.2}Mo_{0.8}N$/Fe–Ni_3N/NF still retain 91% after continuous electrolysis for 50 h, and FE-SEM image of $Ni_{0.2}Mo_{0.8}N$/Fe–Ni_3N/NF demonstrates that the hierarchical and two-dimensional features of the $Ni_{0.2}Mo_{0.8}N$/Fe–Ni_3N/NF remain unchanged after the stability test. As displayed in Fig. 4f, the LSV curves before and after cycle tests also exhibit negligible decrease in current density, suggesting the excellent stability in alkaline condition.

The XRD patterns, XPS survey and XPS spectra of the $Ni_{0.2}Mo_{0.8}N$/Fe–Ni_3N/NF after OER and HER stability test was shown in Fig. S6–S10† and 5. As shown in Fig. S7 and S9,† the diffraction peaks for $Ni_{0.2}Mo_{0.8}N$ (JCPDS 29-0931) both become weaker after the HER and OER stability test, respectively. The XPS survey and XPS spectra of $Ni_{0.2}Mo_{0.8}N$/Fe–Ni_3N/NF after OER and HER all indicate the existences of Ni, Mo, Fe and N elements. The chemical states display small changes, suggesting the superior stability of main structures. The N 1s XPS changes after the HER and OER suggests the surface oxidation of $Ni_{0.2}Mo_{0.8}N$ and the formation of metal-oxyhydroxide or metal-hydroxide. In Fig. 5a, the Ni 2p XPS spectra after stability tests show the BEs of Ni^{3+} (874.5 and 856.8 eV) and Ni^{2+} (872.9 and 855.4 eV).[50] In the Fe 2p XPS spectra (Fig. 5b), the peaks of Fe^{3+} (725.5 and 713.0 eV), Fe^{2+} (722.3 and 709.7 eV) and satellite can be observed.[55] Fig. 5c and d represent the Mo 3d and N 1s spectra after OER test. The peaks of Mo^{6+} 235.0 and Mo^{4+} (233.8 and 230.1 eV), Mo^{3+} (233.0 and 229.0 eV) and N–H bond (399.4 eV), metal–N bond (397.9 eV), Mo–N bond (394.3 eV) can still be observed.[38,49] The chemical states of elements exhibit changes after the OER stability tests, suggesting that the surface of electrocatalyst might be transformed into the metal-oxyhydroxide or metal-hydroxide.[48]

The electrochemical performance of as-synthesized materials toward HER has also been performed. As shown in Fig. 6a and b, the $Ni_{0.2}Mo_{0.8}N$/Fe–Ni_3N/NF displays the best HER activity (40 mV, 20 mA cm^{-2}), which is lower than other electrocatalysts. In addition, the $Ni_{0.2}Mo_{0.8}N$/Fe–Ni_3N/NF also obtains the lowest Tafel slope of 51 mV dec^{-1} (Fig. 6c). The Nyquist plots under HER condition were shown in Fig. 6d. The $Ni_{0.2}Mo_{0.8}N$/Fe–Ni_3N/NF displays a smaller charge-transfer resistance (R_{ct}), indicating that the $Ni_{0.2}Mo_{0.8}N$/Fe–Ni_3N/NF exhibits enhanced charge-transfer ability. The outstanding charge-transfer ability of electrocatalysts for HER lead to favorable electrocatalytic kinetics. Some recently reported HER

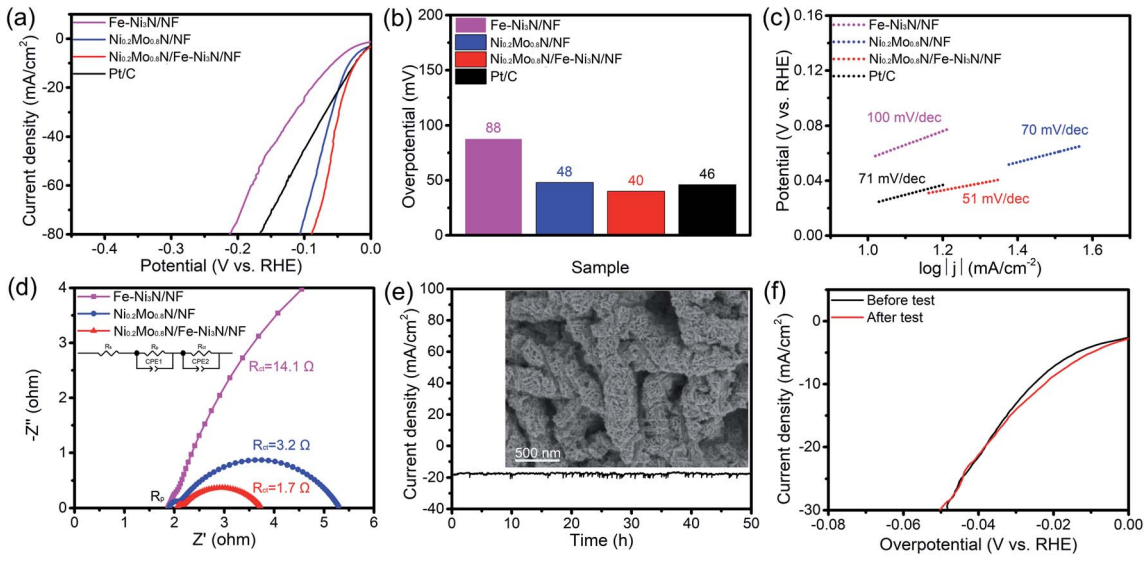

Fig. 6 (a) HER polarization curves of various catalysts. (b) The overpotential of the catalysts obtained at current density of 20 mA cm^{-2}. (c) Tafel slopes of catalysts. (d) EIS spectra of various catalysts recorded at potential of −0.03 V *vs.* RHE. (e) The current–time curves of $Ni_{0.2}Mo_{0.8}N$/Fe–Ni_3N/NF for HER. Inset is the FE-SEM image of $Ni_{0.2}Mo_{0.8}N$/Fe–Ni_3N/NF after HER stability test. (f) The polarization curves of $Ni_{0.2}Mo_{0.8}N$/Fe–Ni_3N/NF before and after continuous stability test.

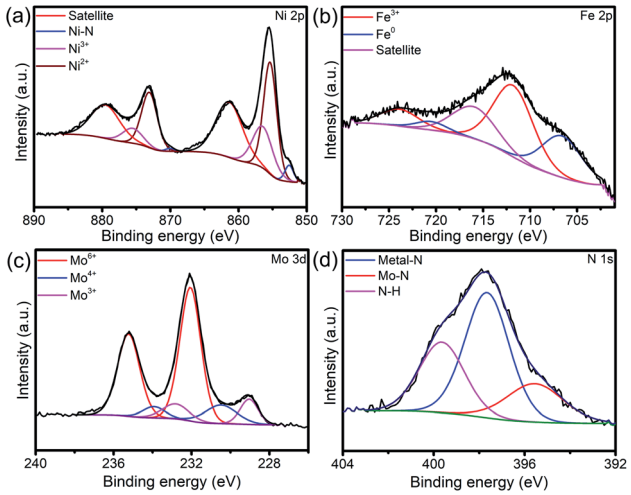

Fig. 7 (a) Ni 2p, (b) Fe 2p, (c) Mo 3d and (d) N 1s XPS spectra of $Ni_{0.2}Mo_{0.8}N/Fe–Ni_3N/NF$ after HER stability test for 50 h.

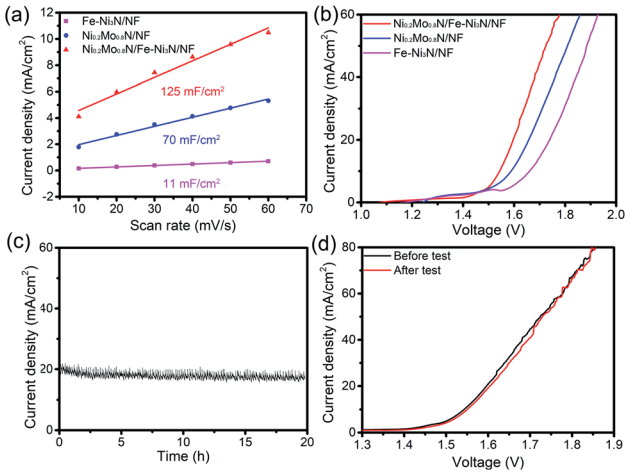

Fig. 8 (a) The electrochemical double-layer capacitances of $Ni_{0.2}Mo_{0.8}N/Fe–Ni_3N/NF$, $Fe–Ni_3N/NF$ and $Ni_{0.2}Mo_{0.8}N/NF$. (b) Overall water splitting polarization curves of two-electrode cell assembled by various catalysts in 1 M KOH solution. (c) The current–time curves of overall water splitting for $Ni_{0.2}Mo_{0.8}N/Fe–Ni_3N/NF$ in KOH solution. (d) Water splitting polarization curves of the initial $Ni_{0.2}Mo_{0.8}N/Fe–Ni_3N/NF$ and the $Ni_{0.2}Mo_{0.8}N/Fe–Ni_3N/NF$ after stability test.

electrocatalyst was summarized in Table S2,† the overpotential of $Ni_{0.2}Mo_{0.8}N/Fe–Ni_3N/NF$ can be comparable. It is noted that the outstanding HER performance of $Ni_{0.2}Mo_{0.8}N/Fe–Ni_3N/NF$ could be ascribed to the strong interactions between $Fe–Ni_3N$ and $Ni_{0.2}Mo_{0.8}N/NF$ phases.

The durability of $Ni_{0.2}Mo_{0.8}N/Fe–Ni_3N/NF$ toward HER was tested at a potential of 74 mV *vs.* RHE. After HER chronopotentiometry test for 50 h, FE-SEM image (Fig. 6e) shows that the hierarchical and two-dimensional features of the $Ni_{0.2}Mo_{0.8}N/Fe–Ni_3N/NF$ remain the same after the HER stability test. The current density of $Ni_{0.2}Mo_{0.8}N/Fe–Ni_3N/NF$ retain 95% (Fig. 6e). The LSV curves (Fig. 6f) of $Ni_{0.2}Mo_{0.8}N/Fe–Ni_3N/NF$ after HER stability tests both show slight difference, suggesting the excellent stability for HER in alkaline condition.

The peak for $Ni_{0.2}Mo_{0.8}N$ phases can be observed from the Fig. S9.† In XPS survey, the signal of N was observed (Fig. S10†). By analyzing the Fig. 7a, the peaks of Ni^{3+} (875.5 and 856.4 eV), Ni^{2+} (873.1 and 855.4 eV) and Ni–N bonds (870.0 and 852.6 eV) can be observed.[45] For the Fe 2p XPS spectra (Fig. 7b), the peaks of Fe^{3+} (723.9 and 711.8 eV) and Fe^0 (720.6 and 706.6 eV) still exist.[52] Furthermore, Mo 3d (Fig. 7c) and N 1s (Fig. 7d) XPS spectra still show the existence of Mo^{6+}, Mo^{4+}, Mo^{3+} and N–H, metal–N, Mo–N.[49] XRD pattern and XPS spectra indicated that the chemical compositions of sample were almost unchanged, revealing the superior stability of $Ni_{0.2}Mo_{0.8}N/Fe–Ni_3N/NF$ in HER process.

The ECSA of various electrocatalysts were roughly obtained by the C_{dl}. The C_{dl} were measured through CVs (Fig. S11†). In Fig. 8a, the C_{dl} of the $Ni_{0.2}Mo_{0.8}N/Fe–Ni_3N/NF$, $Fe–Ni_3N/NF$ and $Ni_{0.2}Mo_{0.8}N/NF$ were 129, 11 and 70 mF cm^{-2}, respectively. The ECSA of the $Ni_{0.2}Mo_{0.8}N/Fe–Ni_3N/NF$, $Fe–Ni_3N/NF$ and $Ni_{0.2}Mo_{0.8}N/NF$ was 1612.5 cm^2, 137.5 cm^2 and 875.0 cm^2, respectively. The bigger C_{dl} and ECSA of $Ni_{0.2}Mo_{0.8}N/Fe–Ni_3N/NF$ demonstrates that the integration of the small $Ni_{0.2}Mo_{0.8}N$ nanosheets on $Fe–Ni_3N$ nanosheets can expose abundant catalytically active site.

Considering the excellent performance of OER and HER and practical applications of the material, $Ni_{0.2}Mo_{0.8}N/Fe–Ni_3N/NF$ was used as the bifunctional electrocatalysts for overall waters splitting. Fig. 8b shows the overall water splitting polarization curves of electrocatalysts. The $Ni_{0.2}Mo_{0.8}N/Fe–Ni_3N/NF$ only requires a potential of 1.54 V to achieve a current density of 10 mA cm^{-2}, which is much smaller than that of $Fe–Ni_3N/NF$ (1.67 V) and $Ni_{0.2}Mo_{0.8}N/NF$ (1.59 V). Furthermore, the $Ni_{0.2}Mo_{0.8}N/Fe–Ni_3N/NF$ bifunctional electrocatalyst shows strong stability, which displayed small degradation after stability test for 20 h (Fig. 8c). The $Ni_{0.2}Mo_{0.8}N/Fe–Ni_3N/NF$ electrode after stability test only need 1.55 V (10 mA cm^{-2}) (Fig. 8d), which further demonstrate its excellent durability.

Conclusions

In summary, we have synthesized a hierarchical, well-organized nanostructure with small $Ni_{0.2}Mo_{0.8}N$ nanosheets grown on the $Fe–Ni_3N$ nanosheets. Compared with the individual $Fe–Ni_3N/NF$ and $Ni_{0.2}Mo_{0.8}N/NF$, the integrated $Ni_{0.2}Mo_{0.8}N/Fe–Ni_3N/NF$ exhibits favorable electrical conductivity, resulting in exceptional performance of OER and HER in alkaline conditions. The experimental results indicated that $Ni_{0.2}Mo_{0.8}N/Fe–Ni_3N/NF$ exhibit superior stability during the OER and HER process. The remarkable electrocatalytic performance and durability of the $Ni_{0.2}Mo_{0.8}N/Fe–Ni_3N/NF$ can be attributed to the optimization of electronic properties under the interaction of $Fe–Ni_3N$ nanosheets and small $Ni_{0.2}Mo_{0.8}N$ nanosheets. Benefit from the excellent chemical performance, stability, and higher ECSA of $Ni_{0.2}Mo_{0.8}N/Fe–Ni_3N/NF$, the as-synthesis material can be used as the efficient electrocatalyst for overall water-splitting in alkaline conditions.

Conflicts of interest

The authors declare no competing financial interests.

Acknowledgements

This study was supported by the National Natural Science Foundation of China (NSFC) (grant no. 51803077, 52073124), Natural Science Foundation of Jiangsu Province (grant no. BK20180627), Postdoctoral Science Foundation of China (2018M630517 and, 2019T120389), the MOE & SAFEA, 111 Project (B13025), the National First-Class Discipline Program of Light Industry Technology and Engineering (LITE2018-19), and the Fundamental Research Funds for the Central Universities (JUSRP221017).

Notes and references

1 P. Kuang, M. Sayed, J. Fan, B. Cheng and J. Yu, *Adv. Energy Mater.*, 2020, **10**, 1903802.
2 J. Cai, J. Shen, X. Zhang, Y. H. Ng, J. Huang, W. Guo, C. Lin and Y. Lai, *Small Methods*, 2019, **3**, 1800184.
3 G. Zhao, K. Rui, S. X. Dou and W. Sun, *Adv. Funct. Mater.*, 2018, **28**, 1803291.
4 P. Li and H. C. Zeng, *ACS Appl. Mater. Interfaces*, 2019, **11**, 46825–46838.
5 Q. Lu, Y. Yu, Q. Ma, B. Chen and H. Zhang, *Adv. Mater.*, 2016, **28**, 1917–1933.
6 M. Gong, D. Y. Wang, C. C. Chen, B. J. Hwang and H. Dai, *Nano Res.*, 2016, **9**, 28–46.
7 B. You and Y. Sun, *Acc. Chem. Res.*, 2018, **51**, 1571–1580.
8 S. Anantharaj, S. R. Ede, K. Karthick, S. S. Sankar, K. Sangeetha, P. E. Karthikc and S. Kundu, *Energy Environ. Sci.*, 2018, **11**, 744–771.
9 J. Duan, S. Chen and C. Zhao, *Nat. Commun.*, 2017, **8**, 1–7.
10 J. Hou, Y. Wu, B. Zhang, S. Cao, Z. Li and L. Sun, *Adv. Funct. Mater.*, 2019, **29**, 1808367.
11 H. Zhu, J. Zhang, R. Yanzhang, M. Du, Q. Wang, G. Gao, J. Wu, G. Wu, M. Zhang, B. Liu, J. Yao and X. Zhang, *Adv. Mater.*, 2015, **27**, 4752–4759.
12 C. Zhu, A. L. Wang, W. Xiao, D. Chao, X. Zhang, N. H. Tiep, S. Chen, J. Kang, X. Wang, J. Ding, J. Wang, H. Zhang and H. J. Fan, *Adv. Mater.*, 2018, **30**, 1705516.
13 X. Du, J. Huang, J. Zhang, Y. Yan, C. Wu, Y. Hu, C. Yan, T. Lei, W. Chen, C. Fan and J. Xiong, *Angew. Chem., Int. Ed.*, 2019, **58**, 4484–4502.
14 Y. Lin, Y. Pan, S. Liu, K. Sun, Y. Cheng, M. Liu, Z. Wang, X. Li and J. Zhang, *Appl. Catal., B*, 2019, **259**, 118039.
15 J. B. Tan and G. R. Li, *J. Mater. Chem. A*, 2020, **8**, 14326–14355.
16 X. Liang, B. Zheng, L. Chen, J. Zhang, Z. Zhuang and B. Chen, *ACS Appl. Mater. Interfaces*, 2017, **9**, 23222–23229.
17 Q. Liang, L. Zhong, C. Du, Y. Luo, J. Zhao, Y. Zheng, J. Xu, J. Ma, C. Liu, S. Li and Q. Yan, *ACS Nano*, 2019, **13**, 7975–7984.
18 G. Ou, P. Fan, H. Zhang, K. Huang, C. Yang, W. Yu, H. Wei, M. Zhong, H. Wu and Y. Li, *Nano Energy*, 2017, **35**, 207–214.
19 V. R. Jothi, R. Bose, H. Rajan, C. Jung and S. C. Yi, *Adv. Energy Mater.*, 2018, **8**, 1802615.
20 Y. Guo, T. Park, J. W. Yi, J. Henzie, J. Kim, Z. Wang, B. Jiang, Y. Bando, Y. Sugahara, J. Tang and Y. Yamauchi, *Adv. Mater.*, 2019, **31**, 1807134.
21 J. Yin, J. Jin, H. Lin, Z. Yin, J. Li, M. Lu, L. Guo, P. Xi, Y. Tang and C. H. Yan, *Adv. Sci.*, 2020, **7**, 1903070.
22 J. Huang, Y. Jiang, T. An and M. Cao, *J. Mater. Chem. A*, 2020, **8**, 25465–25498.
23 S. Anantharaj, S. Kundu and S. Noda, *J. Mater. Chem. A*, 2020, **8**, 4174–4192.
24 W. Chen, X. Hou, X. Shi and H. Pan, *ACS Appl. Mater. Interfaces*, 2018, **10**, 35289–35295.
25 X. Y. Yu, Y. Feng, B. Guan, X. W. Lou and U. Paik, *Energy Environ. Sci.*, 2016, **9**, 1246–1250.
26 G. Zhang, G. Wang, Y. Liu, H. Liu, J. Qu and J. Li, *J. Am. Chem. Soc.*, 2016, **138**, 14686–14693.
27 H. Zhang, A. W. Maijenburg, X. Li, S. L. Schweizer and R. B. Wehrspohn, *Adv. Funct. Mater.*, 2020, **30**, 2003261.
28 Y. Wang, D. Liu, Z. Liu, C. Xie, J. Huo and S. Wang, *Chem. Commun.*, 2016, **52**, 12614–12617.
29 Z. Liu, H. Tan, D. Liu, X. Liu, J. Xin, J. Xie, M. Zhao, L. Song, L. Dai and H. Liu, *Adv. Sci.*, 2019, **6**, 1801829.
30 N. Han, P. Liu, J. Jiang, L. Ai, Z. Shao and S. Liu, *J. Mater. Chem. A*, 2018, **6**, 19912–19933.
31 C. C. Yang, S. F. Zai, Y. T. Zhou, L. Du and Q. Jiang, *Adv. Funct. Mater.*, 2019, **29**, 1901949.
32 J. Jiang, Q. Liu, C. Zeng and L. Ai, *J. Mater. Chem. A*, 2017, **5**, 16929–16935.
33 J. Chen, B. Ren, H. Cui and C. Wang, *Small*, 2020, **16**, 1907556.
34 X. Peng, Y. Yan, X. Jin, C. Huang, W. Jin, B. Gao and P. K. Chu, *Nano Energy*, 2020, **78**, 105234.
35 Z. Zou, X. Wang, J. Huang, Z. Wu and F. Gao, *J. Mater. Chem. A*, 2019, **7**, 2233–2241.
36 F. Ming, H. Liang, H. Shi, X. Xu, G. Mei and Z. Wang, *J. Mater. Chem. A*, 2016, **4**, 15148–15155.
37 C. Ray, S. C. Lee, B. Jin, A. Kundu, J. H. Park and S. C. Jun, *J. Mater. Chem. A*, 2018, **6**, 4466–4476.
38 J. Jia, M. Zhai, J. Lv, B. Zhao, H. Du and J. Zhu, *ACS Appl. Mater. Interfaces*, 2018, **10**, 30400–30408.
39 Y. Gu, S. Chen, J. Ren, Y. A. Jia, C. Chen, S. Komarneni, D. Yang and X. Yao, *ACS Nano*, 2018, **12**, 245–253.
40 L. Zhou, S. Jiang, Y. Liu, M. Shao, M. Wei and X. Duan, *ACS Appl. Energy Mater.*, 2018, **1**, 623–631.
41 S. Sirisomboonchai, S. Li, A. Yoshida, X. Li, C. Samart, A. Abudula and G. Guan, *ACS Sustainable Chem. Eng.*, 2019, **7**, 2327–2334.
42 K. He, T. T. Tsega, X. Liu, J. Zai, X. H. Li, X. Liu, W. H. Li, N. Ali and X. Qian, *Angew. Chem., Int. Ed.*, 2019, **58**, 11903–11909.
43 Y. Zhou, Z. Wang, Z. Pan, L. Liu, J. Xi, X. Luo and Y. Shen, *Adv. Mater.*, 2019, **31**, 1806769.
44 C. Tang, R. Zhang, W. Lu, L. He, X. Jiang, A. M. Asiri and X. Sun, *Adv. Mater.*, 2017, **29**, 1602441.
45 Q. Zhang, D. Yan, Z. Nie, X. Qiu, S. Wang, J. Yuan, D. Su, G. Wang and Z. Wu, *ACS Appl. Energy Mater.*, 2018, **1**, 571–579.

46 Z. Wu, Z. Zou, J. Huang and F. Gao, *J. Catal.*, 2018, **358**, 243–252.
47 J. Lai, B. Huang, Y. Chao, X. Chen and S. Guo, *Adv. Mater.*, 2019, **31**, 1805541.
48 L. Yu, Q. Zhu, S. Song, B. McElhenny, D. Wang, C. Wu, Z. Qin, J. Bao, Y. Yu, S. Chen and Z. Ren, *Nat. Commun.*, 2019, **10**, 1–10.
49 A. Wu, Y. Xie, H. Ma, C. Tian, Y. Gu, H. Yan, X. Zhang, G. Yang and H. Fu, *Nano Energy*, 2018, **44**, 353–363.
50 Z. Wang, P. Guo, S. Cao, H. Chen, S. Zhou, H. Liu, H. Wang, J. Zhang, S. Liu, S. Wei, D. Sun and X. Lu, *Appl. Catal., B*, 2021, **284**, 119725.
51 Y. Wang, C. Xie, D. Liu, X. Huang, J. Huo and S. Wang, *ACS Appl. Mater. Interfaces*, 2016, **8**, 18652–18657.
52 Z. Liu, H. Tan, J. Xin, J. Duan, X. Su, P. Hao, J. Xie, J. Zhan, J. Zhang, J. J. Wang and H. Liu, *ACS Appl. Mater. Interfaces*, 2018, **10**, 3699–3706.
53 C. Tang, H. Zhang, K. Xu, Q. Zhang, J. Liu, C. He, L. Fan and T. Asefa, *J. Mater. Chem. A*, 2019, **7**, 18030–18038.
54 Z. Yin, Y. Sun, Y. Jiang, F. Yan, C. Zhu and Y. Chen, *ACS Appl. Mater. Interfaces*, 2019, **11**, 27751–27759.
55 Z. Cai, D. Zhou, M. Wang, S. M. Bak, Y. Wu, Z. Wu, Y. Tian, X. Xiong, Y. Li, W. Liu, S. Siahrostami, Y. Kuang, X. Q. Yang, H. Duan, Z. Feng, H. Wang and X. Sun, *Angew. Chem., Int. Ed.*, 2018, **57**, 9392–9396.